ELECTRONIC SUPPLEMENTARY INFORMATION

Prismatic Ge-rich inclusions in the hexagonal SiGe shell of GaP-Si-SiGe nanowires by controlled faceting

Roberto Bergamaschini,*[a] Rianne C. Plantenga,*[b] Marco Albani,[a] Emilio Scalise,[a] Yizhen Ren,[b] Håkon Ikaros T. Hauge,[b] Sebastian Kölling,[b]† Francesco Montalenti,[a] Erik P. A. M. Bakkers,[b] Marcel A. Verheijen,[b] and Leo Miglio[a]

Details of the Phase-field model

The phase-field expression for the surface chemical potential of the alloy component i (i=Si or Ge), defined in eq. (3) in the main text, is derived as in Refs.1,2:

$$\mu_i = \mu_\varphi + kT\ln c_i$$

with $\mu_\varphi = \delta F/\delta\varphi$, the variational derivative of the surface-energy functional: [3,4]

$$g(\varphi)\mu_\varphi = -\epsilon\nabla\cdot[\gamma\nabla\varphi] + \frac{1}{\epsilon}\gamma W'(\varphi) + -\nabla\cdot\left[\left(\frac{\epsilon}{2}|\nabla\varphi|^2 + \frac{1}{\epsilon}W(\varphi)\right)\nabla_{\nabla\varphi}\gamma\right] + +\beta\left[-\nabla^2\omega + \frac{1}{\epsilon^2}W''(\varphi)\omega\right]$$

$W(\varphi) = 18\varphi^2(1-\varphi)^2$ is a double well potential which stabilizes the separation of the two phases: solid and vacuum. The additional variable ω is defined as $\omega = -\epsilon\nabla^2\varphi + (1/\epsilon)W'(\varphi)$ and it is equivalent to a measure of the surface curvature. This is needed by the Willmore's regularization term, which is multiplied by the corner-energy parameter β. The effect of this term is to account for the corner energy due to the formation of edges with a high curvature, which in the 2D model are the corners of the NW cross-section. Numerically, this term is required in order to solve the sixth order partial differential equation problem, which results when considering a strong anisotropy for the surface energy density γ. Finally, the function $g(\varphi) = 30\varphi^2(1-\varphi)^2$ has the role to improve the convergence to the sharp-interface limit when $\epsilon \to 0$, providing a better numerical stability of the code. The anisotropy of the surface energy density γ is defined as in Ref. 4 through the surface normal $\hat{\boldsymbol{n}} = -\nabla\varphi/|\nabla\varphi|$:

$$\gamma(\hat{\boldsymbol{n}}) = \gamma_0\left[1 - \sum_{\hat{\boldsymbol{m}}_i}^{<11\bar{2}0>,<10\bar{1}0>} a_i\,(\hat{\boldsymbol{n}}\cdot\hat{\boldsymbol{m}}_i)^{\frac{1}{w_\gamma}}\,\Theta(\hat{\boldsymbol{n}}\cdot\hat{\boldsymbol{m}}_i)\right]$$

The $\hat{\boldsymbol{m}}_i$ unit vectors represent the normal directions of all the $\{11\bar{2}0\}$ and $\{10\bar{1}0\}$ facets of the NW. Each of these corresponds to a minimum in the $\gamma(\boldsymbol{n})$ function, as pictured in Fig. 1 of the main text. The a_i parameters quantify the depth of each minimum with respect to 1, while w_γ sets the width of the minima, and it is equal to 0.02 and γ_0 is a scale factor. Θ is a Heaviside function allowing to distinguish the two opposite orientations for each direction $\hat{\boldsymbol{m}}_i$. Since all experiments here discussed, as well as literature ones on lonsdaleite Si, Ge and SiGe shells,[5–8] always show a profile bounded by the six $\{10\bar{1}0\}$ facets only, it is expected that these are more stable than $\{11\bar{2}0\}$ ones. Based on simple geometrical principles of the Wulff construction, a difference of about 15% between the surface energy density of $\{10\bar{1}0\}$ and $\{11\bar{2}0\}$ facets is sufficient to achieve a Wulff shape made of the six $\{10\bar{1}0\}$ sides only. Recent ab-initio calculations[9] for lonsdaleite pure Si and pure Ge show indeed that $\{10\bar{1}0\}$ are energetically favorable than $\{11\bar{2}0\}$, but the reported difference is not sufficient to exclude small segments of the latter in the Wulff shape. In the present study, we then refer to those values, linearly interpolated for a 30% Ge alloy, only for setting the magnitude of γ_0=80 meV/Å^2 and the value of $a_{11\bar{2}0}$=0.1, corresponding to $\gamma_{11\bar{2}0}$=72 meV/Å^2. A lower value of $\gamma_{10\bar{1}0}$=60 meV/Å^2 is instead assumed, setting $a_{10\bar{1}0}$=0.25, so to ensure that the $\{10\bar{1}0\}$ facets are the only appearing in the Wulff shape. This apparent contrast could be explained by admitting that the actual driving force for the faceting transition includes, in addition to the surface energy term, a concordant kinetic contribution[10] enhancing the adatom transfer from $\{10\bar{1}0\}$ to $\{11\bar{2}0\}$ facets. This requires that $\{10\bar{1}0\}$ grow slower than $\{11\bar{2}0\}$ ones, i.e. that their incorporation rate is slower, which is a reasonable hypothesis by considering that $\{11\bar{2}0\}$ are less stable and hence prefer to get covered by additional atoms. Moreover, the assumption of a linear interpolation for estimating the alloy values may be incorrect, and not identically applicable to the two facets and

[a] L-NESS and Department of Materials Science, University of Milano Bicocca, 20125 Milano, Italy.
[b] Department of Applied Physics, Eindhoven University of Technology, Groene Loper 19, 5612AP Eindhoven, The Netherlands.
† Present address: Department of Engineering Physics, École Polytechnique de Montréal, Montréal, Québec, Canada H3C 3A7
* Corresponding authors. E-mail: roberto.bergamaschini@unimib.it (theory)
r.c.plantenga@tue.nl (experiments)

possibly related to different Ge segregation at the topmost layer,[11] in consequence of the different surface structure.

Deposition is supposed to proceed with the same rate on both $\{10\bar{1}0\}$ and $\{11\bar{2}0\}$ facets thus giving a conformal growth of the shell profile, if not modified by surface diffusion. Still, in a continuum framework, in order to preserve the faceted morphology without rounding at the corners, a higher growth rate is to be set for the intermediate orientations in between the facets.[2] This is obtained by setting the local growth rate R as a function of the profile orientation $\hat{\boldsymbol{n}}$, similarly to what done for γ:

$$\mathrm{R}(\hat{\boldsymbol{n}}) = \mathrm{R}_0 \left[1 - \sum_{\hat{\boldsymbol{m}}_i}^{<11\bar{2}0>,<10\bar{1}0>} b\,(\hat{\boldsymbol{n}} \cdot \hat{\boldsymbol{m}}_i)^{\frac{1}{w_{\mathrm{R}}}}\, \Theta(\hat{\boldsymbol{n}} \cdot \hat{\boldsymbol{m}}_i) \right]$$

where, in this case, the depth of each minima is equal to b=0.5 for all the facets and w_{R}=0.01. The scale parameter R_0 is set to 2 nm/s, so to get a facet growth rate of 1 nm/s compatible with the experimental value (0.8-1.3 nm/s depending on the sample).

It is worth noting that the evolution in the simulations is determined by the growth-rate/mobility ratio. As mobility is not known a priori, here we set M_{Ge}=800nm^6/(eV s) and M_{Si}=80nm^6/(eV s) in order to get the best agreement with experiments.

DFT calculation of $(11\bar{2}0)$ and $(10\bar{1}0)$ GaP surface energy

The surface energy calculations are based on the Density Functional Theory (DFT), by exploiting slab geometry and the following equation:

$$\gamma = \frac{1}{2A}\left(E_{slab} - N\,\mu_{GaP}^{bulk}\right)$$

A is the area of the surface, E_{slab} is the total energy of the slab, μ_{GaP}^{bulk} is the energy per GaP unit of the wurtzite bulk GaP. N is the number of GaP units contained in the slab, thus we consider only stoichiometric surfaces. The slabs were made by 13 layers of bulk material and more than 10 layers of vacuum to avoid interactions between the periodic replica in the out-of-plane direction. The generalized gradient approximation (GGA) was used for the exchange–correlation functional.[12] Projected augmented wave (PAW) pseudopotentials[13,14] have been employed, as implemented in the VASP code.[15] The energy cutoff was set to 600 eV and a (4×8×1) or (4×4×1) k-point mesh was used for the $(11\bar{2}0)$ and $(10\bar{1}0)$ slab calculations, respectively, allowing convergence of the total energy of the systems below typically 10 meV.

The initial structures of the $(11\bar{2}0)$ and $(10\bar{1}0)$ surfaces were built by cutting the bulk crystal in the corresponding directions and obtaining surfaces similar to those of wurtzite GaN.[16] The structures were then relaxed until the forces on all atoms were less than 10 meV/Å, and the final atomistic structures are illustrated in Fig. S1.

The surface energy values obtained are listed in Table S1.

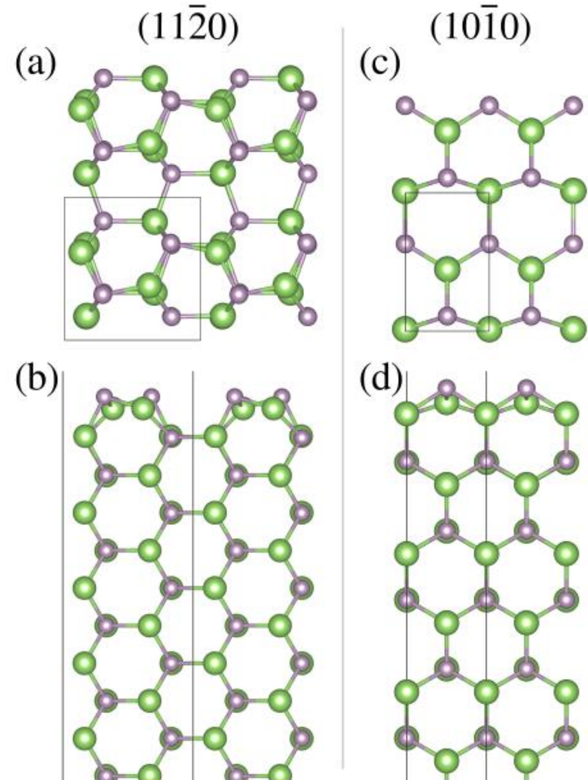

Fig. S1 Atomistic model of the $(11\bar{2}0)$ and $(10\bar{1}0)$ surfaces of the wurtzite GaP, in (a, b) and (c, d), respectively. (a) and (c) are the top view, while (b) and (d) the side view.

Surface	$\boldsymbol{\gamma}$ (meV/Å^2)
$(11\bar{2}0)$	40.90
$(10\bar{1}0)$	39.94

Table S1 Surfaces energy calculated for the $(11\bar{2}0)$ and $(10\bar{1}0)$ surfaces of GaP.

Elastic strain calculations

The elastic strain in the nanowires is estimated by solving the mechanical equilibrium problem via finite element method simulations, using the COMSOL Multiphysics® commercial software. Calculations are performed in 3D by modelling the entire structure of the nanowire, here considered 500 nm long in order to reduce the computational cost. Dirichlet boundary conditions are imposed on one side to reproduce the interaction with the substrate. The simulated structure consists of a 100 nm GaP core, surrounded by a 10 nm Si layer and a SiGe shell. All properties of the SiGe alloy are computed by exploiting the linear Vegard's law. The lattice parameters used are: a = 3.8419 Å and c = 6.3353 for GaP, a = 3.82421 Å

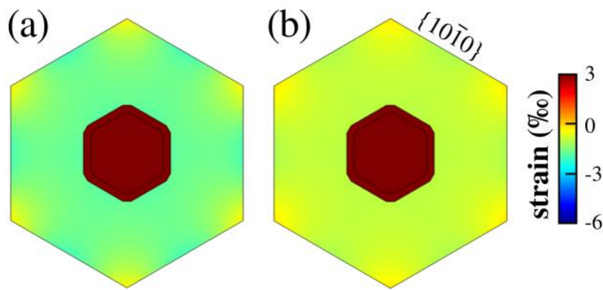

Fig. S2 Color maps of the hydrostatic strain in the (0001) cross section of a GaP-Si-SiGe core-shell nanowire with shell Ge content of (a) 50% and (b) 30%. The GaP core is 100nm large, the Si spacer is 10 nm thick and the SiGe shell is 100nm, similar to experiments of Fig. 2 and 3 of the main text.

and c = 6.3237 for Si, a = 4.05821 Å and c = 6.5877 for Ge. The elastic constants for the hexagonal phase are calculated from the ones for the cubic phase found in Ref. 17, according to Ref. 18.

Simulation results are reported in the Fig. S2 for a 100-nm-thick SiGe shell with (a) 50% and (b) 30% (uniform) Ge content. The color map shows the hydrostatic strain (average of the main strain components xx, yy and zz). The low values of strain, of few per thousands, show the great efficacy of the nanowire configuration in releasing strain. The strain level is approximately the same within the whole shell, but for slightly lower values at the facet edges. Notice that the single strain components can result in values up to ±1%.

In order to assess the possible impact of strain in the formation of the Ge-rich prisms discussed in the main text, in Fig. S3 we repeated the strain calculation for a 10-nm-thick SiGe shell, so to consider the early growth stages at which prisms develop, and vary the morphology. In case (a), we just consider a $\{10\bar{1}0\}$ faceting as in Fig. S2 and observe an enhancement in strain relaxation at the facet edges. In the cases (b) and (c) we instead introduce $\{11\bar{2}0\}$ facets, where the prisms form experimentally, to test whether they correspond to regions of lower strain. Evidently, the favorable strain relaxation found at the facet edges of case (a) is dramatically reduced in case (b) with short $\{11\bar{2}0\}$ facets and becomes almost negligible when larger $\{11\bar{2}0\}$ facets are present, as shown in case (c). The only reduction in strain is then found at the very edge between $\{10\bar{1}0\}$ and $\{11\bar{2}0\}$ facets while a similar strain is found in the middle of both facets. While the situation of case (a) could return a lower elastic chemical potential at the edges, triggering a segregation of Ge, this effect is definitely not the driving force for the prisms formation observed in the Figs. 2 and 3 of the main text, where $\{11\bar{2}0\}$ facets are extended and hence do not

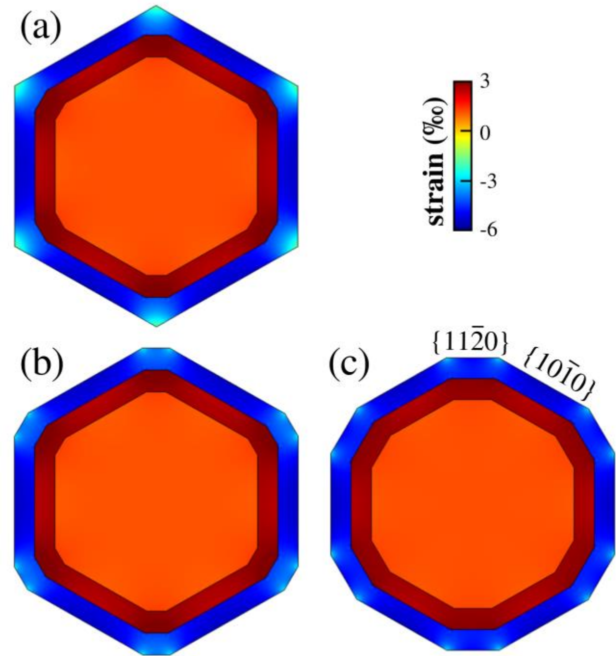

Fig. S3 Color maps of the hydrostatic strain in the cross section of a GaP-Si-SiGe core-shell nanowire. The GaP core is 100nm large, the Si spacer is 10nm thick and the SiGe shell is 10nm, mimicking an early growth stage. A Ge content of 30% is considered. Three different geometries are considered, differing for the presence and size of the $\{11\bar{2}0\}$ facets.

profit from any benefit in the chemical potential compared to the $\{10\bar{1}0\}$ ones.

VLS-GaP vs. VS-GaP growth morphologies

The morphology of the inner GaP core, GaP shell and Si-rich spacer layer have been analyzed by cross-sectional HAADF-STEM. A representative view where the three regions are distinguishable by HAADF contrast is reported in the Fig. S4. Noticeably, the two GaP regions are distinguishable by a slightly different contrast possibly due to unintentional differences (e.g. impurities) due to the different growth process. The inner GaP core NW is indeed grown by gold-catalyzed vapor-liquid-solid (VLS) process while the outer GaP shell is obtained by vapor-solid (VS) deposition. This contrast makes evident a key difference in the faceting, highlighted in the Figure by marker lines. The GaP core NW typically exhibits a $\{10\bar{1}0\}$ faceting with small or absent $\{11\bar{2}0\}$ planes at their corners. The GaP shell instead is characterized by the coexistence of both facets, with rather comparable sizes. Importantly, $\{11\bar{2}0\}$ facets are formed during the VS growth even at corners where they are not present at all at the GaP core profile.

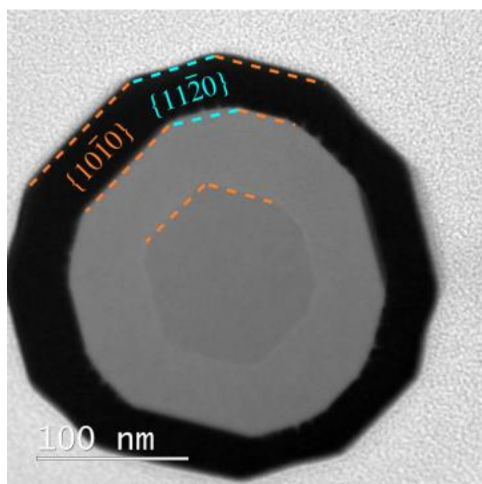

Fig. S4 Cross-section view of the GaP-GaP-Si system imaged in HAADF mode. Markers lines are traced to highlight the appearance of $\{11\bar{2}0\}$ facets in the outer GaP (and Si) shell by VS growth, also at corners where they are not observed at the inner GaP core interface (obtained by VLS growth).

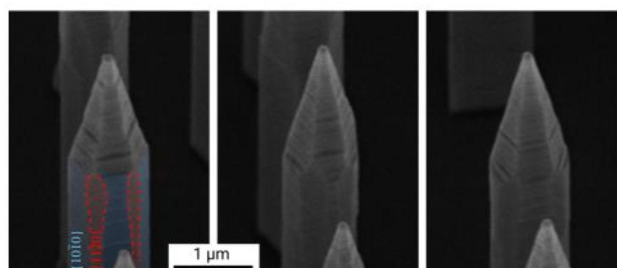

Fig. S5 Cut-out of SEM images of three GaP-GaP core-shell NWs in which the GaP shell was grown by VS for 45 min. The coexistence of both $\{10\bar{1}0\}$ and $\{11\bar{2}0\}$ facets on the NW sidewalls is distinguishable and made evident by dashes at their boundaries in the left image.

To further confirm the connection between the VS GaP shell growth and the formation of $\{11\bar{2}0\}$ facets a separate sample was grown by extending the shell deposition to a much longer time, i.e. 45 minutes vs. the 0.5 and 4 min considered for the previous cases. The presence and persistence of both $\{10\bar{1}0\}$ and $\{11\bar{2}0\}$ facets, made evident in the Fig. S5, demonstrates the robustness of the formation process.

Additional data on EDX analysis

In Figure S6, the individual EDX mappings of Ga, P, Si and Ge are shown for the very same asymmetric NW cross-section of Fig. 3 in the main text. The separation between the core and the shells is rather sharp as no Ga and P are detected in outer SiGe shell as well as no Si and Ge are introduced in the GaP core region (the detection limit for the present EDX

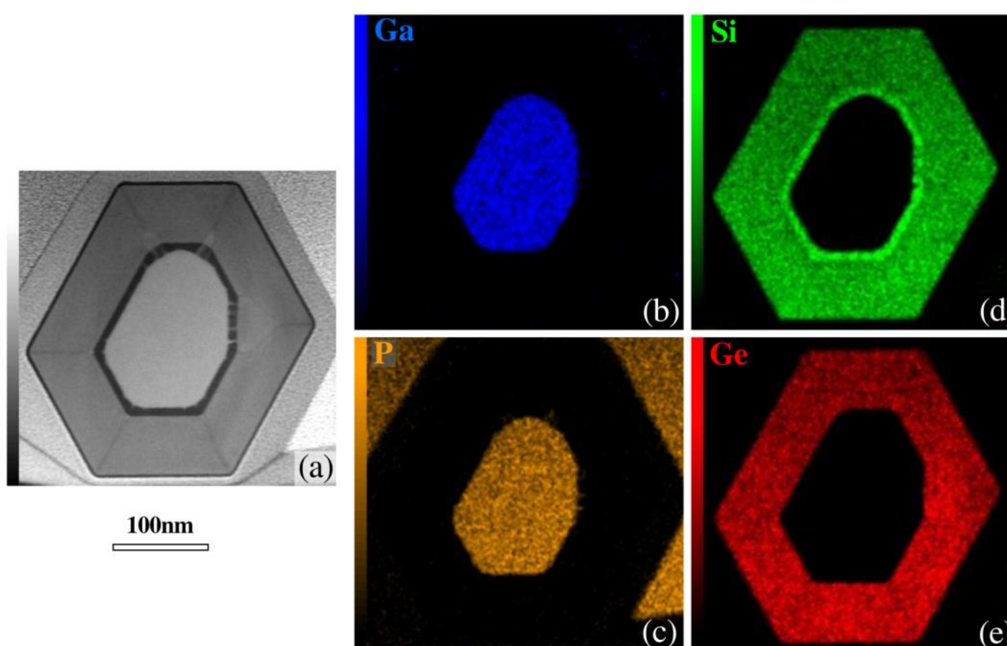

Fig. S6 (a) Cross-section view of the GaP-GaP-Si system imaged in HAADF mode (same as Figure 3 of the main text). Elemental distribution mapping by EDX for (b) Ga-K line, (c) P-K line, (d) Si K-line and (e) Ge K-line over the same cross section. The signal revealed in the outer region of panel (c) corresponds to the Pt coating deposited around the NW prior to FIB preparation of the cross-sectional TEM sample, as the Pt-M line overlaps to the P-K line.

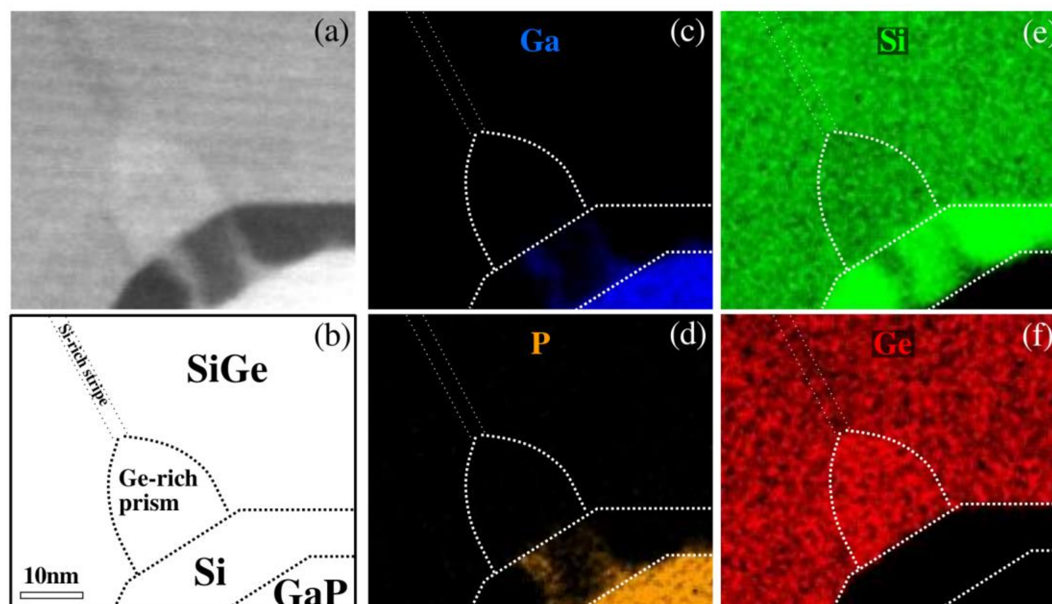

Fig. S7 (a) Magnification of the HAADF cross-section of Fig. S6, in the upper-left corner at the GaP-Si-SiGe interface. (b) Schematics of the different domains as traced by the contrast in panel (a). Elemental analysis by EDX mapping for (c) Ga, (d) P, (e) Si and (f) Ge. Dotted lines are shown for distinguishing the different domains as in panel (b). Notice the presence of GaP-spikey protrusions within the Si layer, below the $\{11\bar{2}0\}$ prism base, not penetrating the outer shell region.

measurements is of the order of few atomic %). Previous Atom Probe Tomography (APT) studies in Ref. 19 showed about 0.5% Ga and 1% P in the close vicinity of the core/shell interface, still not resulting from inter-diffusion. This confirms that the formation of the Ge-rich prisms is not affected by any Ga and P contamination that may interfere with the segregation mechanism and impact on the local properties.

A more accurate analysis reveals that some Ga and P spikey protrusions may appear within the Si inner shell, interestingly, only in correspondence of the $\{\mathbf{11\bar{2}0}\}$ facets. This is made more evident in the magnified views of Fig. S7, where the EDX maps are reported for the GaP-Si-SiGe interface region in correspondence to one prism. Nanometer-thin GaP spikes are recognizable in the Si layer, which is made evident by the dotted marker lines, right below the prism, but they are fully confined there, without any detectable trace in the outer SiGe shell. GaP spikes are evident only in the case of large $\{\mathbf{11\bar{2}0}\}$ facets while at smaller ones only local dents appear at the GaP-Si interface, interesting only at tiny Si thickness (see e.g. the bottom corners of Fig. S6(a) or Fig. S4). While the origin of this behavior is not yet clear, it is worth noticing that it only interests the less stable $\{\mathbf{11\bar{2}0}\}$ facets, while at the $\{\mathbf{10\bar{1}0}\}$ ones the interfaces look sharp without any GaP penetration. Anyway, the fact that such local Ga-P protrusions never continue in the SiGe layer indicates that they do not impact on the segregation dynamics resulting in the Ge-rich prisms, as discussed in the main text.

TEM structural characterization

In order to confirm the wurtzite-hexagonal crystalline phase of the GaP-Si-SiGe core shell nanowires presented in this paper, we performed dedicated TEM analysis along the NW axis for the very same samples reported in the manuscript. To this purpose, we had to prepare a cross-sectional TEM sample, as the core/shell nanowires are too thick to be transparent to the electron beam. Therefore, using Focused Ion Beam (FIB) preparation a cross-sectional (XS) sample was created parallel to the long axis of a nanowire. The section was cut such that the core is included in the TEM lamella. The outcome is summarized in the figure below, showing both a representative diffraction pattern of a ~0.5 micron diameter area of the XS sample and HR-STEM images at the atomic scale, in agreement with the previous observations in literature for both the GaP core[20,21] and the Si/SiGe shells.[5,6]

The crystal structure of the whole NW is hexagonal and no polytype inclusions are observed neither in the III/V core nor in the group IV shells. This is verified for lengths of hundreds of nanometers along the NW axis. Defects are instead observable. These defects are basal stacking faults, previously referred to as ‘cracks’.[21,22]

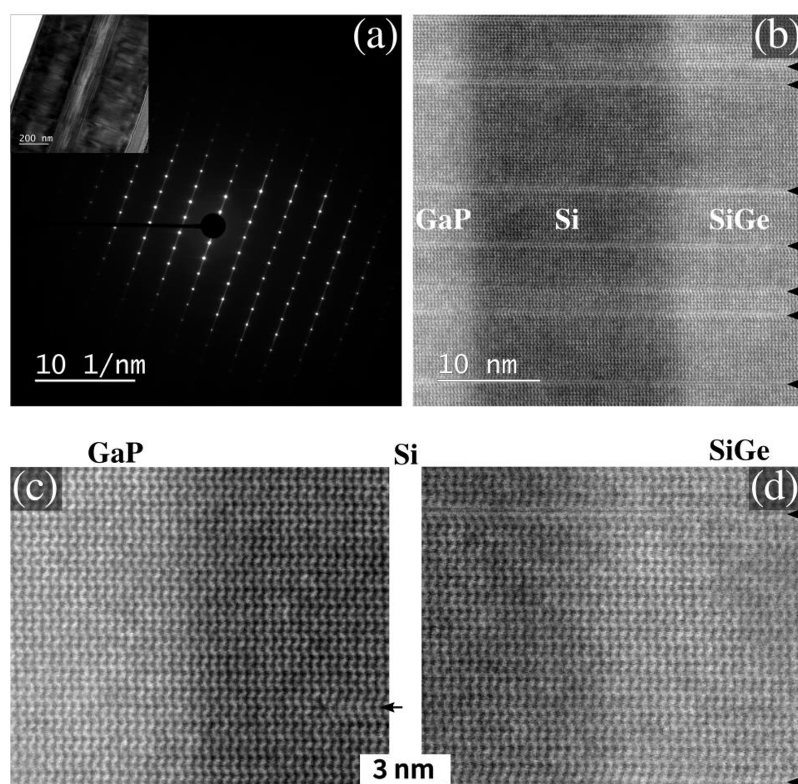

Fig. S8 (a) Selected area electron diffraction pattern of a ~0.5 micron diameter area, displaying a characteristic <11-20> hexagonal phase zone axis pattern. (b) HAADF-STEM image acquired along a <11-20> zone axis displaying the GaP/Si/SiGe core/shell/shell interfaces. Arrows indicate the positions of planar defects. (c, d) more detailed HAADF-STEM images of the GaP/Si and Si/SiGe interfaces, respectively, displaying the ABAB stacking characteristic for the hexagonal phase.

References

1 R. Backofen, R. Bergamaschini and A. Voigt, *Philos. Mag.*, 2014, **94**, 2162–2169.

2 R. Bergamaschini, F. Montalenti and L. Miglio, *Appl. Surf. Sci.*, 2020, **517**, 146056.

3 B. Li, J. Lowengrub, A. Rätz and A. Voigt, *Commun. Comput. Phys.*, 2009, **6**, 433–482.

4 M. Salvalaglio, R. Backofen, R. Bergamaschini, F. Montalenti and A. Voigt, *Cryst. Growth Des.*, 2015, **15**, 2787–2794.

5 H. I. T. Hauge, M. A. Verheijen, S. Conesa-Boj, T. Etzelstorfer, M. Watzinger, D. Kriegner, I. Zardo, C. Fasolato, F. Capitani, P. Postorino, S. Kölling, A. Li, S. Assali, J. Stangl and E. P. A. M. Bakkers, *Nano Lett.*, 2015, **15**, 5855–5860.

6 H. I. T. Hauge, S. Conesa-Boj, M. A. Verheijen, S. Koelling and E. P. A. M. Bakkers, *Nano Lett.*, 2017, **17**, 85–90.

7 Y. Ren, P. Leubner, M. A. Verheijen, J. E. M. Haverkort and E. P. A. M. Bakkers, *Nanotechnology*, 2019, **30**, 295602.

8 E. M. T. Fadaly, A. Dijkstra, J. R. Suckert, D. Ziss, M. A. J. van Tilburg, C. Mao, Y. Ren, V. T. van Lange, K. Korzun, S. Kölling, M. A. Verheijen, D. Busse, C. Rödl, J. Furthmüller, F. Bechstedt, J. Stangl, J. J. Finley, S. Botti, J. E. M. Haverkort and E. P. A. M. Bakkers, *Nature*, 2020, **580**, 205–209.

9 E. Scalise, A. Sarikov, L. Barbisan, A. Marzegalli, D. B. Migas, F. Montalenti and L. Miglio, *Appl. Surf. Sci.*, 2021, 148948.

10 M. Albani, R. Bergamaschini, M. Salvalaglio, A. Voigt, L. Miglio and F. Montalenti, *Phys. status solidi*, 2019, **256**, 1800518.

11 Y. Tu and J. Tersoff, *Phys. Rev. Lett.*, 2004, **93**, 216101.

12 J. P. Perdew, K. Burke and M. Ernzerhof, *Phys. Rev. Lett.*, 1996, **77**, 3865–3868.

13 P. E. Blöchl, *Phys. Rev. B*, 1994, **50**, 17953–17979.

14 G. Kresse and D. Joubert, *Phys. Rev. B*, 1999, **59**, 1758–1775.

15 G. Kresse and J. Furthmüller, *Phys. Rev. B*, 1996, **54**, 11169–11186.

16 J. Neugebauer, in *Nitride Semiconductors*, Wiley-VCH Verlag GmbH & Co. KGaA, Weinheim, FRG, 2006, pp. 295–318.

17 https://www.ioffe.ru/SVA/NSM/Semicond/.

18 R. M. Martin, *Phys. Rev. B*, 1972, **6**, 4546–4553.

19 S. Koelling, R. C. Plantenga, H. I. T. Hauge, Y. Ren, A. Li, M. A. Verheijen, S. Conesa Boj, S. Assali, P. M. Koenraad and E. P. A. M. Bakkers, *ECS Trans.*, 2016, **75**, 751–760.

20 S. Assali, I. Zardo, S. Plissard, D. Kriegner, M. A. Verheijen, G. Bauer, A. Meijerink, A. Belabbes, F. Bechstedt, J. E. M. Haverkort and E. P. A. M. Bakkers, *Nano Lett.*, 2013, **13**, 1559–1563.

21 S. Conesa-Boj, H. I. T. Hauge, M. A. Verheijen, S. Assali, A. Li, E. P. A. M. Bakkers and A. Fontcuberta i Morral, *Nano Lett.*, 2015, **15**, 2974–2979.

22 E. Fadaly, A. Marzegalli, Y. Ren, L. Sun, A. Dijkstra, D. De Matteis, E. Scalise, A. Sarikov, M. De Luca, R. Rurali, I. Zardo, J. E. M. Haverkort, S. Botti, L. Miglio, E. P. A. M. Bakkers, M. A. Verheijen, "*Unveiling Planar Defects in Hexagonal Group IV Materials*", submitted